Tunable Optical Properties and the Role of Defects on the Carrier Lifetimes of $Cs_3Sb_2I_9$ Synthesized in Various Solvents

Samuel M. Neguse, Songhak Yoon, Alexander Frebel, Dennis M. Jöckel, Marc Widenmeyer, Stefan Lange, Arnulf Rosspeintner, Stefan G. Ebbinghaus, Christian Hagendorf, Benjamin Balke, and Anke Weidenkaff*

Pb-free halide perovskites have recently attracted immense attention due to the number of advantages in their optical and electronic properties. However, tuning the optical bandgap with minimized amounts of point defects is a particularly challenging task in photovoltaics. It is pivotal to clearly understand the detailed relationship between the bandgap change with defect generation and charge carrier lifetime. In this study, $Cs_3Sb_2I_9$ crystals are synthesized by varied choice of solvents, namely, γ-butyrolactone, a mixture of dimethylformamide and dimethyl sulfoxide, and hydroiodic acid. Although the same principles of decreasing solubility and crystallization are applied, $Cs_3Sb_2I_9$ crystals with different size and shape in microscopic and macroscopic scale are obtained during heating and cooling of the solution. The synthesized crystals are investigated using a combination of different spectroscopies including Raman, UV–visible, and time-resolved photoluminescence. In the results, it is suggested that there is a strong relationship between Urbach energy and the lifetime of charge carriers. In this research, readily applicable practical principles and examples of how to control the defects for the advancement in Pb-free perovskite photovoltaics are provided.

1. Introduction

Silicon-based solar cells are approaching their expected efficiency limit and intense research efforts have been devoted toward breakthroughs in the development of emerging photovoltaic absorbers.[1–5] Halide perovskites have been identified and emerged as one of the most promising photovoltaic materials due to their power conversion efficiency (PCE) enhancement.[6,7] Particularly, Pb-based halide perovskite solar cells have made rapid progress in the last decades.[8–10] For instance, single-junction solar cells based on formamidinium lead triiodide ($FAPbI_3$) have achieved PCE exceeding 22%.[11] The advancement in Pb-based halide perovskite photovoltaics has been ascribed to facile synthesis, enhanced light absorption, and high defect tolerance as well as longer diffusion lengths and extended lifetimes of charge carriers.[12] However, two main critical challenges that need to be tackled are their instability toward moisture and the toxicity of Pb.[13–16] To commercialize halide perovskite solar cells, Pb needs to be either substituted by less toxic elements to resolve the toxicity issue or encapsulated to solve the imperative problem of stability issue.[17] Another emerging research direction has been persued to explore Pb-free perovskite solar cells. Nontoxic elements such as tin (Sn), bismuth (Bi), and germanium (Ge) have been considered as well as Sb-based

S. M. Neguse, S. Yoon, A. Frebel, D. M. Jöckel, B. Balke, A. Weidenkaff
Energy Materials
Fraunhofer Research Institution for Materials Recycling and Resource Strategies IWKS
Aschaffenburger Straße 121, 63457 Hanau, Germany
E-mail: song.hak.yoon@iwks.fraunhofer.de

M. Widenmeyer, A. Weidenkaff
Department of Materials and Earth Sciences
Technical University of Darmstadt
Peter-Grünberg-Straße 2, 64287 Darmstadt, Germany

The ORCID identification number(s) for the author(s) of this article can be found under https://doi.org/10.1002/adpr.202300184.

S. Lange, C. Hagendorf
Diagnostics and Metrology of Solar Cells
Fraunhofer Centre for Silicon Photovoltaics CSP
Otto-Eißfeldt-Strasse 12, 06120 Halle (Saale), Germany

A. Rosspeintner
Department of Physical Chemistry
University of Geneva
Quai Ernest Ansermet 30, CH-1211 Geneva 4, Switzerland

S. G. Ebbinghaus
Institute of Chemistry
Martin Luther University Halle-Wittenberg
Kurt-Mothes-Strasse 2, 06120 Halle (Saale), Germany

perovskites.[18–20] These have gained further attention, due to their suitable bandgap for single-junction solar cells.[21] In particular $Cs_3Sb_2I_9$ has been shown to be a promising candidate for various optoelectronic applications including solar cells, photodetectors, light-emitting diodes, photocatalysts, and resistive switching memory.[22–29] For instance, pressure induced bandgap engineering, forced degradation studies with different environmental conditions, and the reversible thermochromic behavior have been investigated.[22,30–32] $Cs_3Sb_2I_9$ can be formed either in a layered 2D structure or in a dimer 0D structure.[33] The 2D materials are expected to perform better in terms of efficiency for solar cell application compared to 0D materials.[34] This is also supported by the bandgap values reported with an indirect bandgap of 2.30 eV for the 0D and direct bandgap of 2.05 eV for the 2D $Cs_3Sb_2I_9$.[31]

In this study, we primarily focus on exploring the effects of different solvents and synthesis methods on the optical properties of $Cs_3Sb_2I_9$ crystals with different size and shape on microscopic and macroscopic scale. The solvents used in this study were γ-butyrolactone (GBL), a 7:3 mixture of dimethylformamide and dimethyl sulfoxide (DMF/DMSO), and strong hydroiodic (HI) acid solution. GBL is widely used in the synthesis of various halide perovskites, especially for iodide-based systems.[35–37] In addition, GBL is regarded as less toxic than DMF/DMSO.[38] The solvents DMF and DMSO were widely used to dissolve the precursors.[39,40] Zhang et al. utilized the mixture of DMF and DMSO for a successful synthesis of $Cs_3Bi_2I_9$, and the same approach was applied for the $Cs_3Sb_2I_9$ system.[41] Alternatively, HI acid is widely used for the synthesis of $Cs_3Sb_2I_9$ crystals providing an abundant and easily accessible source for iodide in water. After the synthesis, the resulting crystals were analyzed with Raman spectroscopy and X-ray diffraction (XRD) for phase identification. Microstructural characterization of the crystals was carried out by scanning electron microscopy (SEM). UV–visible (UV–vis), steady-state, and time-resolved photoluminescence (PL) spectroscopic measurements were conducted to find the correlation between defect structure and optical properties of $Cs_3Sb_2I_9$.

2. Results

For the purpose of phase identification Raman spectroscopy was used as it is highly sensitive to local crystal structure and symmetry.[42] **Figure 1** shows the normalized Raman spectra of the synthesized crystals. The spectra were normalized to the most intense band (131 cm^{-1}), which allows to analyze the position and broadening of the other bands. The $Cs_3Sb_2I_9$ crystal structure was confirmed for all four samples synthesized under different experimental conditions. All spectra exhibited seven distinctive Raman peaks at around 52, 63, 95, 110, 131, 146, and 171 cm^{-1}.[43] No additional bands were observed within the measured range of 50–1500 cm^{-1}, revealing that the local crystal structures of the four samples are not different from each other. The spectra did not show any major deviations in peak positions or intensities. The relative intensity of the bands decreases in the order DMF/DMSO_fast > GBL_slow > GBL_fast > HI_fast except for the band at around 52 cm^{-1} as shown in Figure 1. The full width at half maximum (FWHM)
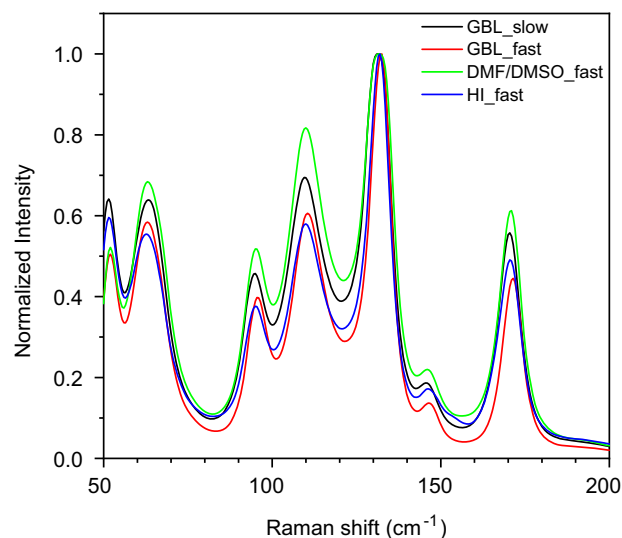

Figure 1. Normalized Raman spectra of the synthesized $Cs_3Sb_2I_9$ crystals.

of the band at around 131 cm^{-1} was evaluated to investigate the degree of crystal imperfections or defects in the $Cs_3Sb_2I_9$ crystal lattice. A higher FWHM value indicates a higher concentration of imperfections or defects leading to Sb–I bond vibrations with broken local symmetry. The resulting FWHM values were 7.54, 6.44, 7.19, and 6.62 cm^{-1} for GBL_slow, GBL_fast, DMF/DMSO_fast, and HI_fast, respectively. The FWHM values indicate that GBL_fast and HI_fast showed better crystallinity compared to GBL_slow and DMF/DMSO_fast.

$Cs_3Sb_2I_9$ was confirmed for all samples by Raman spectroscopy. However, a precise determination and differentiation of polymorphs by Raman spectroscopy were limited. In this regard, for further characterization, the crystal structure was analyzed by XRD and a selected 2θ range of the patterns is shown in **Figure 2**. All reflections of the four samples can be assigned to the 2D-layered structure with space group $P\bar{3}m1$ (JCPDS-PDF No. 98-003-9822). An extended XRD patterns and details of the unit cell parameters derived from the Le Bail fitting are shown in Supporting Information S1. The peak at $2\theta = 32.2°$ in GBL_slow belongs to CsI, which was not found in the other samples synthesized by the hydrothermal method. Evidently, it can be inferred that only finite amount of CsI can be soluble during the heating up the solution in GBL even though an extremely slow ramping to 95 °C with 2 °C day^{-1} was applied to grow crystals. Thus, hydrothermal synthesis seems more favorable for getting $Cs_3Sb_2I_9$ crystals. In addition, the peak at $2\theta = 29.9°$ only found in HI_fast is a signature of the 0D dimer phase as this peak is absent in the layered phase. This peak was not found in the other samples synthesized by the organic solvents.[44] In general, it is not justifiable to distinguish different phases from just one reflection in XRD. However, when $Cs_3Sb_2I_9$ phase of 2D-layered structure with space group $P\bar{3}m1$ and that of 0D dimer phase with space group $P6_3/mmc$ (JCPDS-PDF No. 98-000-1447) are compared, the peak at $2\theta = 29.9°$ can be a fingerprint of the 0D dimer phase. The other peak at $2\theta = 32.2°$ that belongs to 0D dimer that should be absent for 2D-layered structure unfortunately overlaps with CsI phase (JCPDS-PDF
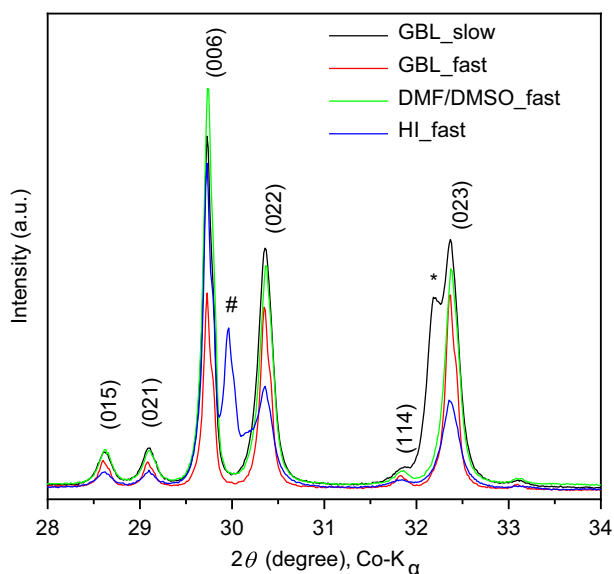
Figure 2. X-ray diffraction patterns of γ-butyrolactone (GBL)_slow, GBL_fast, dimethylformamide and dimethyl sulfoxide (DMF/DMSO)_fast, and hydroiodic acid (HI)_fast. * indicates CsI (JCPDS-PDF No. 98-008-4989) and # indicates the existence of 0D dimer $Cs_3Sb_2I_9$ (JCPDS-PDF No. 98-000-1447).

No. 98-008-4989). Therefore, in a given condition of XRD data obtained, the peak at $2\theta = 29.9°$ could be a good indicator for the existence of 0D dimer phase formed only in HI_fast. In previous papers, it has been reported that only the 0D dimer form crystallizes from HI solution.[22,31–33] In contrast, in our synthesis, the 2D-layered phase is formed together with the 0D one in HI_fast.

The difference in crystal size and morphology depending on the synthesis conditions is evident from **Figure 3**. The depicted SEM images reveal that GBL_fast consists of well-defined hexagonal crystals (Figure 2b), whereas highly agglomerated and irregular-shaped crystals are found for GBL_slow even though nucleation and crystal growth were well controlled by an extremely slow solution heating. The SEM image from DMF/DMSO_fast showed much less defined irregular particles mixed with hexagonally shaped crystals. Lastly, the most well-defined and the largest crystals were obtained in case of HI_fast. While the crystals from the organic solvents reveal more platelike or irregular morphology, the crystals originating from HI are several times larger in size and smoother on the surface.

Different colors of the crystals were observed depending on the utilized solvents. GBL_slow and GBL_fast had an orange color, while DMF/DMSO_fast and HI_fast exhibited a very dark red color as shown in Supporting Information S2. UV–vis absorbance spectra converted from the measured reflectance spectra are shown in **Figure 4**. The absorption edges for both samples synthesized in GBL can be found at around 600 nm, while DMF/DMSO and HI samples showed a shifted absorption edge to higher wavelength at around 660 nm. Interestingly, for HI_fast a second band edge was observed at around 670 nm.[32] Reportedly, antimony-based perovskites usually tend to form a 0D dimer structure in solution-processed synthesis instead of 2D-layered structure.[32] The indirect optical bandgaps were estimated to be 2.11, 2.00, 2.12, and 1.85 eV for GBL_slow, GBL_fast, DMF/DMSO_fast, and HI_fast, respectively. The HI_fast exhibited the smallest bandgap. The Urbach energies E_U determined by plotting the logarithmic absorption against
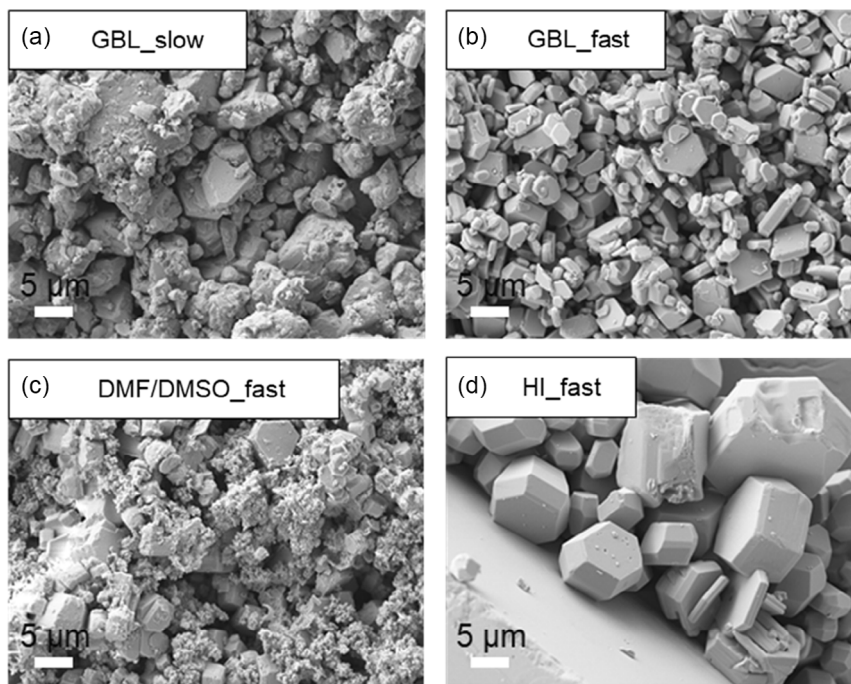

Figure 3. Scanning electron microscopy images of $Cs_3Sb_2I_9$ crystals synthesized in different solvents: a) GBL_slow, b) GBL_fast, c) DMF/DMSO_fast, and d) HI_fast.

**ADVANCED
SCIENCE NEWS**

www.advancedsciencenews.com

**ADVANCED
PHOTONICS
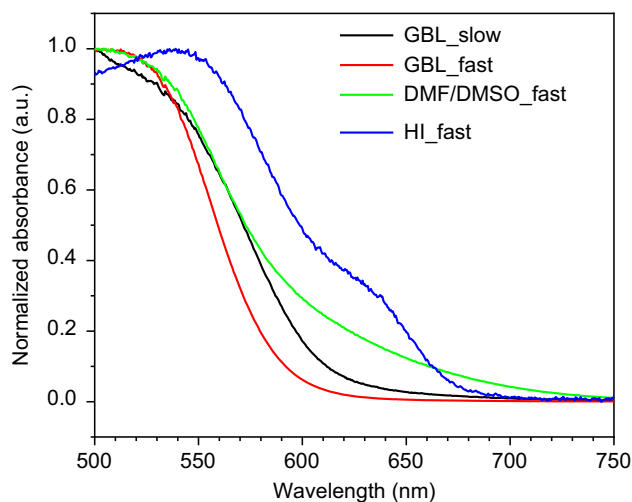RESEARCH**
Open Access

www.adpr-journal.com

Figure 4. UV–visible absorption spectra of GBL_slow, GBL_fast, DMF/DMSO_fast, and HI_fast.

the photon energy and then taking the reciprocal of the slope[45,46] were 118.2, 69.2, 158.8, and 251.4 meV for GBL_slow, GBL_fast, DMF/DMSO_fast, and HI_fast, respectively. E_U is one of the indicators for crystal imperfections including lattice defects.[47,48] Ledinsky et al. have found that E_U is 3.8 ± 0.7 meV for $CH_3NH_3PbI_3$, which is smaller than that of Si, GaAs, InP, or GaN, highlighting the remarkable optoelectronic properties of Pb-based iodide perovskite.[47] Hence, E_U is regarded as a good figure of merit to show the potential of a newly discovered light absorber. A higher E_U reflects a higher structural disorder or higher amounts of defects in the crystal. It should be noted that the lowest bandgap and highest E_U of HI_fast was observed among all four samples. Unexpectedly, GBL_fast exhibited almost two times lower E_U than GBL_slow. Controlled slow solution heating (GBL_slow) did not result in reduced concentration of defects.

PL spectroscopy was performed (Supporting Information S3) to obtain a better understanding of the photoexcitation and photoemission characteristics of $Cs_3Sb_2I_9$. The emission peaks of maximum intensity are found to be slightly lower than those reported in literature.[42,49] The PL peak of GBL_slow exhibited a redshift compared to those of three other samples. Obvious conclusion to explain this has not been reached yet and future study would be needed. Moreover, the emission peak is asymmetric and broad for all samples. The origin of asymmetry is attributed to several factors such as the electron–phonon coupling, the defect states in the band structure, or self-trapped excitons.[43,50]

The lifetime of charge carriers was measured and estimated by time-resolved PL (TR-PL) at the band edge emission. The results are shown in **Figure 5**a as a log–log scale plot. These decay curves were fitted with a double-exponential decay (Equation (1)).

$$I(t) = A_1 \exp\left(\frac{-t}{\tau_1}\right) + A_2 \exp\left(\frac{-t}{\tau_2}\right) \tag{1}$$

where t is the time, A_1 and A_2 are pre-exponential factors, and τ_1 and τ_2 are the corresponding decay times for the exponential components, respectively. The fitted results of the lifetimes of
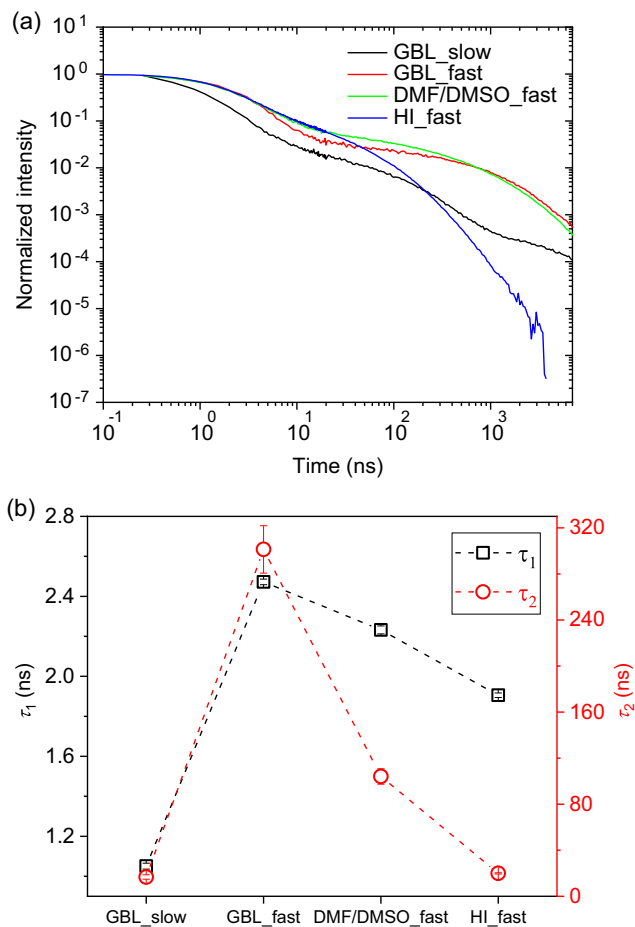

Figure 5. a) Time-resolved photoluminescence (TR-PL) spectra on a double-logarithmic scale and b) decay parameters τ_1 and τ_2 from TR-PL.

τ_1 and τ_2 for each sample are shown in Figure 5b. The decay constants for τ_1 are in the range of 1–3 ns, similar to the values reported by Wang et al.[51] The τ_2 decay time is in a much broader range of 15–300 ns. By comparing the decay times τ_1, it can be concluded that GBL_slow showed a much shorter charge carrier lifetime for τ_1 indicating faster recombination processes and hampering the process of charge transfer. In contrast, the other three samples synthesized by the hydrothermal method showed almost two times longer τ_1 compared to GBL_slow. The three different solvents used for the hydrothermal synthesis resulted in a broad range of the τ_2 decay times.

3. Discussion

$Cs_3Sb_2I_9$ has attracted much interest as a potential photovoltaic absorber to replace Pb-based halide perovskites. However, there are critical issues and several inherent limitations that hamper the utilization of $Cs_3Sb_2I_9$ in solar cells. First of all, dimensionality matters. This is also one of the reasons why the reported Pb-free perovskite and perovskite derivative photovoltaics (0D, 1D, and 2D structures) have shown inferior PCE compared to Pb-based halide perovskite photovoltaics (3D structure).[52] Two polymorphs of $Cs_3Sb_2I_9$, namely 0D dimer phase and

2D-layered one, were reported in 1997.[33] The variation of the Sb–I octahedral network structure results in an inevitable change of the optoelectronic properties of $Cs_3Sb_2I_9$.[22,44] Depending on the crystal growth conditions, different crystal structures are formed. The 0D dimer form was mainly found for samples synthesized from HI solution at relatively low temperatures,[32] whereas the 2D-layered phase is formed in solid-state reactions,[33] colloidal synthesis of nanocrystals,[31,53] and HCl-assisted solution methods.[54] The increased pressure during the hydrothermal synthesis applied in this study may be the decisive difference compared to the synthesis conditions reported in literature. Compared to organic solvents (GBL or DMF/DMSO), the HI aqueous solution exhibited a decreased solubility when the temperature decreased leading to nucleation and crystal growth. Thus, the crystals synthesized by hydrothermal method using HI aqueous solution (HI_fast) resulted in well-defined big (more than 10 μm) and thick crystals, even though the cooling rate was the fastest among all. Moreover, 0D- and 2D-phase mixtures were identified by XRD for HI_fast in this study. This phase mixture can be linked to two absorption bands in UV–vis spectroscopy. Further study is essential to obtain a deeper understanding of the synthesis condition in HI aqueous solution and its resulting crystal formation of $Cs_3Sb_2I_9$ polymorph.

Concerning the bandgap value of the 2D-layered $Cs_3Sb_2I_9$ phase, mostly values of 2.05–2.10 eV are reported.[21,26,44] By substitution of Sb, a much smaller bandgap of 1.63 eV was obtained for $Cs_3Bi_{0.6}Sb_{1.4}I_9$.[51] In our study, the bandgaps of the $Cs_3Sb_2I_9$ crystals were in good agreement with the reported values of 2D $Cs_3Sb_2I_9$ except HI_fast for which a slightly lower value of 1.85 eV was obtained due to the existence of the second band edge observed at around 670 nm. By density-functional theory calculation, V'_{Cs}, I'_i, $Cs^{\bullet}_i$, $I^{\bullet\bullet\bullet}_{Sb}$, and $V^{\bullet}_I$ are found to be dominant defects in $Cs_3Sb_2I_9$. I'_i, $I^{\bullet\bullet\bullet}_{Sb}$, and $V^{\bullet}_I$ are generally expected to be a possible source of charge carrier traps.[21] X-ray photoelectron spectroscopy (XPS) measurements were carried out to investigate the Cs/Sb and (Cs+Sb)/I ratios of the synthesized $Cs_3Sb_2I_9$ and the results are summarized in Supporting Information S4. No observable difference was found in Cs/Sb ratio. However, DMF/DMSO_fast showed that the (Cs+Sb)/I ratio is approximately four times higher than that of HI_fast ($\approx$2.4 vs. $\approx$0.6). Considering the abundant iodide in the synthesis condition, the deep defects do not seem to be resulted from $V^{\bullet}_I$ in HI_fast. HI_fast showed the highest E_U, which implies large amounts of deep defect states that could act as recombination centers. The highest E_U and the shortest τ_2 for HI_fast revealed the existence of different types of defects, such as e.g., stacking faults or a large mosaicity. The carrier lifetime of $Cs_3Sb_2I_9$ needs to be improved to enhance the PCE, and one of the major remaining challenges is the fundamental understanding of defect formation in this material. The change of (Cs+Sb)/I ratio could not be fully understood and further studies would be necessary to address this issue in more detail. The findings are summarized in Supporting Information S5.

4. Conclusion

The crystal structural and optical properties of $Cs_3Sb_2I_9$ crystals grown from various solvents (GBL, a mixture of DMF/DMSO,

and HI) were investigated. Different colors of crystals are obtained depending on the solvent used. $Cs_3Sb_2I_9$ crystals of mixed 0D dimer and 2D-layered crystal structures could be grown in HI solution by hydrothermal synthesis revealing the highest Urbach energy with the shortest charge carrier lifetime. In contrast, $Cs_3Sb_2I_9$ synthesized in GBL by hydrothermal synthesis revealed the lowest Urbach energy but the longest charge carrier lifetime. Thus, GBL is found to be not only more ecologically feasible for the whole device fabrication compared to acidic solvent, but also more necessarily suitable within the investigated hydrothermal synthesis condition with enhanced optical properties. Fundamental understandings of solvent role in $Cs_3Sb_2I_9$ can also provide further information about the various synthesis route of other Sb-based halides. Future work should focus on upgrading synthesis methods for industrial applications.

5. Experimental Section

Synthesis of $Cs_3Sb_2I_9$ Crystals: Crystals were grown by changing the solubility which depends strongly on temperature and pressure.[55] The Cs_3SbI_9 crystals were synthesized using an oil bath on a hot plate. To produce a clear precursor solution, 6 mmol CsI (Alfa Aesar, 99.9%) and 4 mmol SbI_3 (Alfa Aesar, 99.9%) were dissolved in 10 mL GBL (Sigma-Aldrich, Technipur, for synthesis). The reaction vessel with the precursor solution was capped to prevent evaporation of the solvent and a small hole was drilled in the cap to release the increased pressure during heating. The oil bath was heated to 80 °C with stirring and then held for 1 day. Afterward, an extremely slow ramping to 95 °C with 2 °C day^{-1} was applied to grow crystals. After reaching 95 °C, the grown crystals were separated from the GBL solution and dried on a filter paper. They are denoted as GBL_slow in the following. In addition to this slow crystal growth method, microwave-assisted hydrothermal synthesis was applied for a faster crystal growth. Microwave digestion system Turbowave 1500 (MLS Mikrowellen-Labor-Systeme GmbH) was used. 6 mmol CsI and 4 mmol SbI_3 were dissolved in 10 mL GBL. The starting precursor together with GBL solution were put in a Teflon-lined autoclave and placed in the microwave system. The autoclave was heated up to 90 °C in 10 min with a pressure of 4.7 MPa and kept under these conditions during a dwell time of 1 h. Then, the solution was heated up to 105 °C in 5 h where the heating rate was fast (3 °C h^{-1}) compared to the one using the oil bath (2 °C day^{-1}). The crystals were then instantly separated by decanting the solution. The grown crystals were dried on a filter paper and are denoted as GBL_fast. In a separate experiment, a 7:3 mixture of DMF (Sigma-Aldrich, for peptide synthesis) and DMSO (Sigma-Aldrich, anhydrous, $\geq$99.9%) was used for hydrothermal synthesis. The 6 mmol CsI and 4 mmol SbI_3 were dissolved in 7 mL DMF and 3 mL DMSO under the same hydrothermal conditions. These crystals were named DMF/DMSO_fast. When HI was used for hydrothermal synthesis, 3 mmol CsI and 2 mmol SbI_3 were dissolved in 5 mL HI aqueous solution (48 wt%, Alfa Aesar). The solution was heated to 200 °C for 10 min with a pressure of 4.7 MPa and then cooled down to room temperature in 1 h. The cooling rate thus was rather fast in this experiment (150 °C h^{-1}). Again, the grown crystals were separated by decantation and dried on a filter paper. These crystals are denoted as HI_fast.

Characterization of $Cs_3Sb_2I_9$ Crystals—Raman Spectroscopy: Raman spectra were recorded at room temperature using a Bruker SENTERRA Raman Microscope. An excitation wavelength of 632.8 nm (He-Ne laser) was applied with a resolution of 2–5 cm^{-1}. An objective lens with a magnification of 20 and an aperture of 25 μm was chosen. The spectral resolution was 0.5 cm^{-1} in a measured range of 50–1500 cm^{-1}.

XRD: The powder XRD patterns were obtained using a Co-source diffractometer (Malvern PANalytical Empyrean, Co-K$\alpha_{1,2}$ radiation) to identify the phases present in the synthesized Cs_3SbI_9 samples. The diffraction

patterns were recorded in a 2θ range of 20° and 100° with an angular step interval of 0.013°.

SEM: The particle sizes and their size distribution and morphology were studied by a field-emission SEM (Carl Zeiss) equipped with an X-Max large-area energy dispersive spectroscopy (EDS) detector (Oxford Instruments) operating at an accelerating voltage of 5 kV.

UV–Vis Spectroscopy: UV–vis diffuse reflectance spectra were acquired using a Perkin Elmer Lambda 900 spectrometer equipped with a deuterium arc lamp for UV light and a tungsten–halogen lamp for visible and near-infrared light. The baseline measurement was taken with $BaSO_4$ as white standard. The spectra were recorded with a scan speed of 500 nm min^{-1} in the wavelength range from 1000 to 200 nm. The obtained reflectance spectra were converted to absorbance using the Kubelka–Munk function $F(R)$ (Equation (2)).

$$\alpha \approx F(R) = \frac{(1 - R)^2}{2R} \tag{2}$$

where α is the absorbance and R the reflectance.[56] The bandgaps were calculated using the Tauc plot method.[11] In addition, the Urbach energy interpreted as one of the indicators for the amount of localized states in the optical bandgap and for crystal imperfections[57] was determined by plotting $\ln(\alpha)$ against photon energy (Equation (3)).

$$\alpha(E) = \alpha_0 \exp\left(\frac{h\nu}{E_U}\right) \tag{3}$$

PL Spectroscopy and TR-PL: The PL emission spectra were obtained at room temperature using a spectrofluorometer (Fluorolog 3-2iHR, Horiba) with an R5509-73 PMT as detector. All spectra were corrected for photometric response. The spectra were measured in front face geometry with the powder/microcrystals being mounted between 2 quartz plates. The excitation wavelength was set to 440 nm. For TR-PL experiments, the samples were excited with the output of a pulsed laser diode (437 nm, PicoQuant LD-440) with approximately 1 pJ on a spot with a diameter (using the $1/e$ definition) of approximately 30 µm resulting in fluence of ≈ 100 nJ cm^{-2}. The repetition rate of the light source was 31.3 kHz. The polarization of the excitation was controlled using a Glan–Taylor polarizer and set to s-polarization. Fluorescence of the samples (mounted between microscope plates) was collected using a Cassegrain-type collection optic (Anagrain; Anaspec Research Laboratories Ltd., Berkshire, UK) in 180° back-scattering geometry, passed through a long-pass filter (488 nm, IDEX/Semrock), a wire-grid polarizer (Thorlabs, WP25M-UB) at magic angle with respect to the excitation, and focused onto a fiber/fiber-bundle using an achromatic lens (Thorlabs, AC254-100-AB). The fiber output was directly focused on a single-photon avalanche diode (Micro Photon Devices, MPD-100-CTE) with the help of an elliptic mirror (Horiba, 1427C). The time-correlated single-photon counting was established using a PicoHarp-300 (PicoQuant).

XPS: XPS was performed in a Kratos Axis Ultra DLD instrument, equipped with a monochromatic Al-Kα source ($E = 1486.6$ eV). An analysis area of 300×700 µm was defined by an electrostatic–magnetic lens system. Sample charging was suppressed by a low-energy electron flood gun. Survey spectra between 1330 and −5 eV binding energy were recorded with an analyzer pass energy (PE) of 80 and 0.5 eV energy step width. Core level and valence band detail spectra were recorded with a PE of 10 eV and energy step width of 0.1 and 0.025 eV, respectively. For acquisition of depth profiles and for removal of contaminations, the surface was gradually sputter-eroded by a 500 eV Ar$^+$ ion beam with a beam current density in the order of 10 µA mm^{-2}.

Supporting Information

Supporting Information is available from the Wiley Online Library or from the author.

Conflict of Interest

The authors declare no conflict of interest.

Data Availability Statement

The data that support the findings of this study are available in the supplementary material of this article.

[1] H. Xiang, P. Liu, W. Wang, R. Ran, W. Zhou, Z. Shao, *Chem. Eng. J.* **2021**, *420*, 127599.

[2] C. N. Savory, A. Walsh, D. O. Scanlon, *ACS Energy Lett.* **2016**, *1*, 949.

[3] X. Yang, W. Wang, R. Ran, W. Zhou, Z. Shao, *Energy Fuels* **2020**, *34*, 10513.

[4] G. Volonakis, A. A. Haghighirad, R. L. Milot, W. H. Sio, M. R. Filip, B. Wenger, M. B. Johnston, L. M. Herz, H. J. Snaith, F. Giustino, *J. Phys. Chem. Lett.* **2017**, *8*, 772.

[5] A. Furasova, P. Voroshilov, D. Sapori, K. Ladutenko, D. Barettin, A. Zakhidov, A. Di Carlo, C. Simovski, S. Makarov, *Adv. Photonics Res.* **2022**, *3*, 2100326.

[6] B. Parida, A. Singh, A. K. Kalathil Soopy, S. Sangaraju, M. Sundaray, S. Mishra, S. F. Liu, A. Najar, *Adv. Sci.* **2022**, *9*, 2200308.

[7] Q. Wei, M. Ghasemi, R. Wang, C. Wang, J. Wang, W. Zhou, B. Jia, Y. Yang, X. Wen, *Adv. Photonics Res.* **2023**, *4*, 2200236.

[8] N. K. Tailor, M. Abdi-Jalebi, V. Gupta, H. Hu, M. I. Dar, G. Li, S. Satapathi, *J. Mater. Chem. A* **2020**, *8*, 21356.

[9] H. J. Snaith, *J. Phys. Chem. Lett.* **2013**, *4*, 3623.

[10] N. J. Jeon, J. H. Noh, W. S. Yang, Y. C. Kim, S. Ryu, J. Seo, S. I. Seok, *Nature* **2015**, *517*, 476.

[11] J. A. Steele, P. Puech, M. Keshavarz, R. Yang, S. Banerjee, E. Debroye, C. W. Kim, H. Yuan, N. H. Heo, J. Vanacken, A. Walsh, J. Hofkens, M. B. J. Roeffaers, *ACS Nano* **2018**, *12*, 8081.

[12] S. D. Stranks, H. J. Snaith, *Nat. Nanotechnol.* **2015**, *10*, 391.

[13] Y. Rong, Y. Hu, A. Mei, H. Tan, M. I. Saidaminov, S. I. Seok, M. D. McGehee, E. H. Sargent, H. Han, *Science* **2018**, *361*, eaat8235.

[14] A. Babayigit, A. Ethirajan, M. Muller, B. Conings, *Nat. Mater.* **2016**, *15*, 247.

[15] M. Ren, X. Qian, Y. Chen, T. Wang, Y. Zhao, *J. Hazard. Mater.* **2022**, *426*, 127848.

[16] M. A. Green, A. Ho-Baillie, H. J. Snaith, *Nat. Photonics* **2014**, *8*, 506.

[17] H. Chen, C.-R. Zhang, Z.-J. Liu, J.-J. Gong, W. Wang, Y.-Z. Wu, H.-S. Chen, *Mater. Sci. Semicond. Process.* **2021**, *123*, 105541.

[18] M. Chen, M.-G. Ju, H. F. Garces, A. D. Carl, L. K. Ono, Z. Hawash, Y. Zhang, T. Shen, Y. Qi, R. L. Grimm, D. Pacifici, X. C. Zeng, Y. Zhou, N. P. Padture, *Nat. Commun.* **2019**, *10*, 16.

[19] A. Sarkar, P. Acharyya, R. Sasmal, P. Pal, S. S. Agasti, K. Biswas, *Inorg. Chem.* **2018**, *57*, 15558.

[20] E. W.-G. Diau, E. Jokar, M. Rameez, *ACS Energy Lett.* **2019**, *4*, 1930.

[21] B. Saparov, F. Hong, J.-P. Sun, H.-S. Duan, W. Meng, S. Cameron, I. G. Hill, Y. Yan, D. B. Mitzi, *Chem. Mater.* **2015**, *27*, 5622.

[22] L. Wu, Z. Dong, L. Zhang, C. Liu, K. Wang, B. Zou, *ChemSusChem* **2019**, *12*, 3971.

[23] B. Pradhan, G. S. Kumar, S. Sain, A. Dalui, U. K. Ghorai, S. K. Pradhan, S. Acharya, *Chem. Mater.* **2018**, *30*, 2135.

[24] A. Singh, N.-C. Chiu, K. M. Boopathi, Y.-J. Lu, A. Mohapatra, G. Li, Y.-F. Chen, T.-F. Guo, C.-W. Chu, *ACS Appl. Mater. Interfaces* **2019**, *11*, 35088.

[25] L. Wang, Z. Shi, Z. Ma, D. Yang, F. Zhang, X. Ji, M. Wang, X. Chen, G. Na, S. Chen, D. Wu, Y. Zhang, X. Li, L. Zhang, C. Shan, *Nano Lett.* **2020**, *20*, 3568.

[26] N. Lamminen, G. K. Grandhi, F. Fasulo, A. Hiltunen, H. Pasanen, M. Liu, B. Al-Anesi, A. Efimov, H. Ali-Löytty, K. Lahtonen, P. Mäkinen, A. Matuhina, A. B. Muñoz-García, M. Pavone, P. Vivo, *Adv. Energy Mater.* **2022**, *13*, 2203175.

[27] A. Singh, K. M. Boopathi, A. Mohapatra, Y. F. Chen, G. Li, C. W. Chu, *ACS Appl. Mater. Interfaces* **2018**, *10*, 2566.

[28] J.-C. Hebig, I. Kühn, J. Flohre, T. Kirchartz, *ACS Energy Lett.* **2016**, *1*, 309.

[29] H. Wang, B. Zhou, W. Li, *Phys. Chem. Chem. Phys.* **2022**, *25*, 486.

[30] T. Geng, Z. Ma, Y. Chen, Y. Cao, P. Lv, N. Li, G. Xiao, *Nanoscale* **2020**, *12*, 1425.

[31] T. D. Chonamada, A. B. Dey, P. K. Santra, *ACS Appl. Energy Mater.* **2020**, *3*, 47.

[32] A. Singh, S. Satapathi, *Adv. Opt. Mater.* **2021**, *9*, 2101062.

[33] K. Yamada, H. Sera, S. Sawada, H. Tada, T. Okuda, H. Tanaka, *J. Solid State Chem.* **1997**, *134*, 319.

[34] M. I. Saidaminov, O. F. Mohammed, O. M. Bakr, *ACS Energy Lett.* **2017**, *2*, 889.

[35] J. H. Heo, S. H. Im, J. H. Noh, T. N. Mandal, C.-S. Lim, J. A. Chang, Y. H. Lee, H. Kim, A. Sarkar, M. K. Nazeeruddin, M. Grätzel, S. I. Seok, *Nat. Photonics* **2013**, *7*, 486.

[36] W. A. Laban, L. Etgar, *Energy Environ. Sci.* **2013**, *6*, 3249.

[37] M. I. Saidaminov, A. L. Abdelhady, G. Maculan, O. M. Bakr, *Chem. Commun.* **2015**, *51*, 17658.

[38] C. Worsley, D. Raptis, S. Meroni, A. Doolin, R. Garcia-Rodriguez, M. Davies, T. Watson, *Energy Technol.* **2021**, *9*, 2100312.

[39] X. Huang, Z. Zhao, L. Cao, Y. Chen, E. Zhu, Z. Lin, M. Li, A. Yan, A. Zettl, Y. M. Wang, X. Duan, T. Mueller, Y. Huang, *Science* **2015**, *348*, 1230.

[40] N. Ahn, D.-Y. Son, I.-H. Jang, S. M. Kang, M. Choi, N.-G. Park, *J. Am. Chem. Soc.* **2015**, *137*, 8696.

[41] Y. Zhang, Y. Liu, Z. Xu, H. Ye, Z. Yang, J. You, M. Liu, Y. He, M. G. Kanatzidis, S. F. Liu, *Nat. Commun.* **2020**, *11*, 2304.

[42] M. Mala, T. Appadurai, A. K. Chandiran, *Dalton Trans.* **2022**, *51*, 2789.

[43] K. M. McCall, C. C. Stoumpos, S. S. Kostina, M. G. Kanatzidis, B. W. Wessels, *Chem. Mater.* **2017**, *29*, 4129.

[44] S. Paramanik, A. J. Pal, *Adv. Electron. Mater.* **2022**, *8*, 2200211.

[45] C. Ayik, I. Studenyak, M. Kranjec, M. Kurik, *Optics* **2014**, *4*, 76.

[46] N. Falsini, G. Roini, A. Ristori, N. Calisi, F. Biccari, A. Vinattieri, *J. Appl. Phys.* **2022**, *131*, 10902.

[47] M. Ledinsky, T. Schönfeldová, J. Holovský, E. Aydin, Z. Hájková, L. Landová, N. Neyková, A. Fejfar, S. de Wolf, *J. Phys. Chem. Lett.* **2019**, *10*, 1368.

[48] E. Ugur, M. Ledinský, T. G. Allen, J. Holovský, A. Vlk, S. de Wolf, *J. Phys. Chem. Lett.* **2022**, *13*, 7702.

[49] J.-P. Correa-Baena, L. Nienhaus, R. C. Kurchin, S. S. Shin, S. Wieghold, N. T. Putri Hartono, M. Layurova, N. D. Klein, J. R. Poindexter, A. Polizzotti, S. Sun, M. G. Bawendi, T. Buonassisi, *Chem. Mater.* **2018**, *30*, 3734.

[50] H. Lei, D. Hardy, F. Gao, *Adv. Funct. Mater.* **2021**, *31*, 2170217.

[51] G. Chen, P. Wang, Y. Wu, Q. Zhang, Q. Wu, Z. Wang, Z. Zheng, Y. Liu, Y. Dai, B. Huang, *Adv. Mater.* **2020**, *32*, e2001344.

[52] Z. Xiao, Z. Song, Y. Yan, *Adv. Mater.* **2019**, *31*, e1803792.

[53] J. Pal, S. Manna, A. Mondal, S. Das, K. V. Adarsh, A. Nag, *Angew. Chem., Int. Ed.* **2017**, *56*, 14187.

[54] F. Umar, J. Zhang, Z. Jin, I. Muhammad, X. Yang, H. Deng, K. Jahangeer, Q. Hu, H. Song, J. Tang, *Adv. Opt. Mater.* **2019**, *7*, 1801368.

[55] Y. Cho, H. R. Jung, W. Jo, *Nanoscale* **2022**, *14*, 9248.

[56] J. Su, Y. Huang, H. Chen, J. Huang, *Cryst. Res. Technol.* **2020**, *55*, 1900222.

[57] F. Urbach, *Phys. Rev.* **1953**, *92*, 1324.